



UNIVERSITÀ DI PARMA

ARCHIVIO DELLA RICERCA

University of Parma Research Repository

Experimental tests on shear capacity of naturally corroded prestressed beams

This is the peer reviewed version of the following article:

Original

Experimental tests on shear capacity of naturally corroded prestressed beams / Belletti, B.; Rodriguez, J.; Andrade, C.; Franceschini, L.; Sanchez Montero, J.; Vecchi, F.. - In: STRUCTURAL CONCRETE. - ISSN 1464-4177. - 21:5(2020), pp. 1777-1793. [10.1002/suco.202000205]

Availability:

This version is available at: 11381/2886394 since: 2022-01-10T09:28:50Z

Publisher:

Wiley-Blackwell

Published

DOI:10.1002/suco.202000205

Terms of use:

Anyone can freely access the full text of works made available as "Open Access". Works made available

Publisher copyright

note finali coverpage

(Article begins on next page)

17 February 2025

EXPERIMENTAL TESTS ON SHEAR CAPACITY OF NATURALLY CORRODED PRESTRESSED BEAMS

Beatrice Belletti*

Full Professor at Department of Engineering and Architecture, University of Parma
Parco Area delle Scienze 181/A, 43124 Parma, Italy
Tel: +390521905930, Fax: +390521905924
beatrice.belletti@unipr.it

Jesus Rodriguez

Associate Professor at Department of Structures and Physic of Buildings, University Poly-
technic of Madrid (UPM), Madrid, Spain

Carmen Andrade

Visiting Research Professor at International Centre for Numerical Methods in Engineering
(CIMNE), Universitat Politècnica de Catalunya (UPC), Barcelona, Spain

Lorenzo Franceschini

PhD student at Department of Engineering and Architecture, University of Parma

Javier Sánchez Montero

PhD Researcher at Institute Eduardo Torroja of Construction Sciences, Serrano Galvache,
Madrid, Spain

Francesca Vecchi

Post-doctoral research fellow at at Department of Engineering and Architecture, University of
Parma

*Corresponding author.

1 **Abstract**

2 An experimental campaign was carried out on full-scale naturally corroded prestressed concrete (PC) beams
3 without transverse reinforcement to investigate the corrosion effects on failure modes, shear capacity and
4 ductility. The analysed PC beams, structural members of a thermal power plant, were subjected for 10 years
5 to refrigerating wetting cycles with marine water. In this paper, the experimental results of four-point bending
6 tests, carried out at the Institute “Eduardo Torroja” in Madrid, are described. Before tests, a visual inspection
7 was conducted to detect the damages induced by corrosion. During the tests, displacements and strains
8 were measured by using Linear Variable Displacement Transducer (LVDT) and Digital Image Correlation
9 (DIC). After the tests, strands were removed from beams and cut in pieces, which were weighed to measure
10 the mass loss. Lastly, it was proved that the residual life of PC beams, exposed to chloride attack, is strongly
11 affected by corrosion, whose effects reduce the shear capacity both in terms of resistance and ductility.

12
13 **Keywords**

14 Prestressed concrete beams, shear capacity, natural corrosion, Digital Image Correlation.

15 **1. INTRODUCTION**

16 In the last years, corrosion has been considered as one of the main factors that causes detrimental effects
17 on durability and resistance of reinforced concrete (RC) and prestressed concrete (PC) structures and infra-
18 structures. After the recent bridge collapses occurred worldwide, such as the Ynys-y-gwas Bridge in 1985 in
19 Port Talbot (Woodward and Williams, 1988), the Santo Stefano Bridge in 1999 in Sicily, the Annone over-
20 pass in 2016 in Veneto, the Fossano Bridge in 2017 in Piemonte, the Morandi Bridge in 2018 in Liguria (Di
21 Prisco, 2019), and the highway overpass in 2019 in Wuxi, extensive surveys on infrastructures were
22 planned. Surveys outcomes revealed that many RC and PC existing structures are reaching - or already
23 reached - the end of their service life and they show evidences of corrosion and deterioration. Research car-
24 ried out in the United State by the American Society of Civil Engineers (ASCE) and the Federal Highway Ad-
25 ministration (FHWA) report that the 9% of the USA bridges were classified as “structural deficient” and that
26 the 30% of existing bridges have already exceeded their service life (Soltani et al.,2019). Moreover, environ-
27 mental degradation can be considered the cause of more than the 7% of bridge collapses occurred from
28 1980 to 2012 (Di Prisco,2019). Therefore, in order to plan maintenance, repairing or dismantlement actions
29 is fundamental to properly evaluate the effects of corrosion-induced mechanisms on RC and PC structures
30 and infrastructures.

31 In case of environment-exposed structures, carbonation-induced corrosion, chloride-induced corrosion, or
32 corrosion-induced by chloride additives into concrete can cause damage (Zhou et al., 2014). Corrosion leads
33 to damage in concrete, such as cracking and spalling of cover caused by volume expansion, reinforcement
34 cross-section reduction due to rust products formation and loss of mechanical performances of steel. Usu-
35 ally, chloride-induced corrosion can be more dangerous in prestressed members because pitting can cause
36 damage localization and localised failures of members. Since the environmental aggressive attack - due to
37 chloride contents or carbonatation - is increasing over the time, the capacity of corroded RC or PC existing

38 members is gradually reducing, sometime causing unexpected failures due to lack of bending, shear or an-
39 chorage resistance. In this paper, the shear capacity reduction of prestressed reinforced concrete beams
40 without transverse reinforcement subjected to chloride-induced corrosion is analysed.

41 In case of laboratory test specimens, corrosion can be naturally triggered or artificially accelerated by apply-
42 ing an electrical potential. In general, the artificially accelerated method produces different corrosion effects
43 than those induced by the natural environmental attack on structures. In this paper, PC beams subjected to
44 natural chloride-induced corrosion caused by the exposure to refrigeration wetting cycles, executed by using
45 seawater, are analysed.

46 Experimental tests on corroded RC beams are available in literature. Soltani et al. (2019) pointed out that
47 112 specimens were tested from 1955 to 2017 to investigate the shear capacity of RC members with cor-
48 roded reinforcement. However, most of the research deals with beams with transverse reinforcement. Hig-
49 gins and Farrow (2006) tested nine corroded beams and five reference beams and proved that the reduction
50 of the area of stirrups, caused by corrosion, lead to localised yielding and durability's reduction. Juarez et al.
51 (2011) tested eight corroded and eight reference beams and demonstrated that corrosion affects both re-
52 sistance and ductility of the beams. Lachemi et al. (2014) tested twelve corroded RC beam and four uncor-
53 roded beams and stated that, for low levels of corrosion - corresponding to a mass loss of about 5% - shear
54 capacity is reduced by 5% to 25%, while for high level of corrosion - corresponding to a mass loss of about
55 20% - shear capacity is reduced by 50% to 75%. Rodriguez et al. (1997) tested 30 RC beams and found that
56 for 14 corroded beams shear failure was anticipated to bending failure due to pitting at stirrups of 6 mm in
57 diameter. Then, as soon as a stirrup failed, a diagonal crack failure occurred, as in beams without web rein-
58 forcement. Some proposals on how to deal with shear capacity of RC corroded elements (beams and slabs)
59 are available in Contecvet Manual (2001). Contecvet Manual states that for element with web reinforcement,
60 the shear capacity can be estimated assuming the reduced steel and concrete sections; while for elements
61 without web reinforcement, due to the relevance of loss of bond, sometimes, the shear capacity assessment
62 requires to move from "beam action" to "arch action" schematisation.

63 Despite a large amount of papers reports results of tests carried out on RC beams, only few papers provide
64 experimental data on the shear capacity of corroded PC beams. Rinaldi et al. (2010) carried out four-point
65 bending tests on nine artificially corroded PC beams and pointed out that corrosion affects the ultimate flex-
66 ural capacity, the failure mode and finally the structural response of PC beams. **Recupero et al. (2019) tested**
67 **a set of prestressed beams artificially corroded.** In this paper, the results of an experimental campaign, which
68 investigates the shear capacity of corroded PC beams, are illustrated.

69 The few experimental papers, which are available in literature, on the shear capacity of PC beams, provide
70 test results of artificially corroded beams with shear reinforcement. Therefore, the main novelty of this re-
71 search is in the presentation of experimental test results on critical shear naturally corroded prestressed
72 beams without transverse reinforcement. **Weight loss of prestressing reinforcement reduces the reinforce-**
73 **ment ratio, that in turn affects the shear transfer in the shear crack and in the uncracked compression zone**
74 **(Marí et al., 2015; Cavagnis et al., 2018; Classen, 2020).** In this paper, an experimental campaign on seven
75 full-scale naturally corroded prestressed beams and one reference beam is presented. The experimental
76 programme involved PC beams subjected to a natural corrosive environment for 10 years. The level of corro-
77 sion of strands was evaluated by measuring the mass loss of some pieces of strands extracted from the
78 beams. The non-linear behaviour of PC beams, subjected to four-point bending tests, is described by plotting

79 load vs deflection curves and measurements obtained from Digital Image Correlation (DIC). These latter
80 measurements are presented in terms of maximum principal strain values and deformed profiles of the PC
81 beams for different levels of the applied load.

82 The results presented in this paper can contribute populating database of experimental results on corroded
83 members. Furthermore, the presented results can be useful for the calibration of reliable analytical and nu-
84 merical models capable of predicting the capacity of corroded PC beams, in terms of both resistance and
85 ductility, and the corresponding failure mode, (Mora et al., 2018; Belletti et al., 2019; Mora et al., 2019). In-
86 deed, in order to optimise the maintenance strategies of the existing structural heritage, design methods ca-
87 pable of inputting the outcomes from in-situ inspections and outputting corroded members' capacity and re-
88 sidual life estimation are needed.

89 **2. EXPERIMENTAL PROGRAMME**

90 Fourteen naturally corroded and two uncorroded PC beams were tested at the “Instituto de Ciencias de la
91 Construcción Eduardo Torroja” in Madrid. The PC beams had the same geometric and mechanical proper-
92 ties and came from a refrigeration tower of a thermal power plant. During their lifecycle the PC beams were
93 subjected to the chlorides attack induced by the refrigeration wetting cycles executed using seawater. **The**
94 **beams, when they were in service, were simply supported on a precast concrete beams.**

95 Two experimental campaigns were performed from March 2018 to June 2019. During the first experimental
96 campaign, carried out from March to June 2018, eight corroded and two uncorroded PC beams were tested,
97 while the other six corroded PC beams were tested during the second campaign performed from March
98 to June 2019.

99 In this paper, the shear capacity of seven naturally corroded PC beams and one reference uncorroded beam
100 is investigated, while the flexural capacity of two naturally corroded PC beams and one reference uncor-
101 roded beam is illustrated in Belletti et al. (2020).

102 **3. MATERIALS and METHOD**

103 **3.1. Design of test specimens**

104 The full-scale prestressed beams were characterised by a rectangular cross-section having width, b , equal to
105 150 mm and height, h , equal to 300 mm.

106 The prestressing reinforcement consisted of two seven wires strands 1/2 S having an equivalent diameter
107 equal to 12.9 mm, placed at the bottom of the cross-section. The yield strength, $f_{p0.1k}$, was equal to 1580
108 MPa, while the nominal ultimate strain, ϵ_u , was equal to 5%. An initial prestressing strength, σ_p , equal to 1408
109 MPa was applied to PC beams. The top longitudinal reinforcements consisted of two $\Phi 5$ steel ribbed bars.
110 The beams were built without transverse reinforcement and the **distance of the centroid of the reinforcement**
111 **from the outer surface** was equal to 40 and 50 mm, respectively, for the reinforcement placed at the top and
112 at the bottom of the cross-section of the beam. Figure 1 shows the beams geometry and reinforcement de-
113 tails. Table 1 reports the mechanical properties of the steel, as indicated in the design drawings of the
114 beams.

115 Cylindrical concrete compressive strength, f_{cm} , was estimated from destructive compressive tests performed
116 on cores extracted - after failure - from specimens PB4P9, PB4P13 and PB4P14. From each beam, four cy-
117 lindrical samples 100 mm high and with a diameter equal to 50 mm were extracted. Compressive uni-axial
118 tests were performed by using an Autamax 5 machine, working at a load rate equal to 0.6 MPa/s. Finally, a
119 mean value of concrete compressive strength equal to 45.4 MPa was obtained.
120 Before tests, several damages due to corrosion of strands were visible, such as concrete cover spalling in
121 proximity to the beams' ends, longitudinal cracks, and swellings, as shown in Figure 2.

122

123 3.2. Test Set-up

124 All the specimens were subjected to load-control four-point bending tests, which were carried out up to fail-
125 ure by means of a servo-hydraulic actuator with a nominal maximum capacity equal to 200 kN, as shown in
126 Figure 3. The PC beams were simply supported at both ends. The distance between supports, L , is varying
127 depending on beams' damage at their ends. Two symmetrical loads were applied by means of a steel beam
128 at a distance equal to $L/3$ from supports, Figure 3(a). In order to measure the deflection of the beam, a Lin-
129 ear Variable Displacement Transducer (LVDT) was placed at the bottom of the beam at mid-span, as shown
130 in Figure 3(a). The instrumentation was completed with steel plates having dimension 70 mm x 200 mm x 8
131 mm located in correspondence of supports and loading points' positions.

132 The loading points were not symmetric with respect to the beam length because the distances between sup-
133 ports and beam ends, d_1 and d_2 , were not equal due to corrosion damage. Indeed, the supports were placed
134 200 mm far from the corner or, in case of spalling of concrete cover or longitudinal cracks, 200 mm far from
135 the end of the damage. Table 2 summarizes the main geometrical dimensions of the tested PC beam.

136 An identifying code, composed by letters and numbers, is used to name the beams: PB means prestressed
137 beam and 4P means four-point bending test, Table 2. Furthermore, the letter N is added after the abbrevia-
138 tion PB to denote the uncorroded specimen (reference beam). Table 2 reports, for each PC beams, the de-
139 tails of the loading setup and the shear span-to-depth ratios, a/d , - being the shear span, a , equal to $L/3$.

140 In this paper, DIC methodology was used to monitor the non-linear behaviour of PC beams during loading up
141 to failure. A high contrast speckle pattern was applied to the beams' surfaces in a region of interest (ROI)
142 delimited by supports, Figure 3(a), and constant illumination was provided in order to avoid interferences
143 caused by the shadow effect. The high-resolution digital camera Nikon D7200 completed the DIC system
144 (24.72 million pixels). Images were post-processed using the open source two-dimension software package
145 Ncorr (Schreier et al., 2009; Tambusay et al., 2018; Blaber et al., 2015), which works in MATLAB environ-
146 nment. The region of interest (ROI) was 300 mm high and with a variable length depending on the distance
147 between supports, as shown in Figure 3(a). The post-processing phase consisted in the comparison of the
148 reference image representing the undeformed shape of the beam - captured before the application of the
149 load - and the images representing the deformed shape of the beam - captured every 5 kN load increment.
150 Displacements and strains values were obtained by overlapping the images of undeformed and deformed
151 beams. In this paper, the contour plot of maximum principal strain values and the deformed beams' profiles
152 for different values of applied load are reported.

153

154 3.3. Corrosion Damage Detection

155 3.3.1. Crack pattern maps

156 Before the four-point bending tests, visual inspections were performed to detect areas damaged by corro-
157 sion, which may be potential zones where brittle failures may occur. Figure 5(a) - Figure 11(a) show longitudi-
158 nal cracks, spalling of concrete cover at beams' ends, and swelling, drawn in their exact location and col-
159 oured in red in the crack pattern maps. The crack pattern map of the uncorroded beam PBN4P2 (reference
160 beam) is not reported because no damage was visible on the beam surface before the test. Figure 4 shows
161 the photo of the beam PBN4P2 at failure.

162 Before tests, spalling of concrete cover at the left end of the beam was visible for PB4P5 and PB4P8 beams,
163 as shown in Figure 5(a) and Figure 8(a). PB4P8 beam presented swelling in correspondence of the right end
164 of the beam.

165 Spalling of concrete cover at both ends was visible for PB4P6 and PB4P7 beams, as shown in Figure 6(a)
166 and Figure 7(a). Furthermore, the crack pattern map of PB4P7 beam shows branched cracks at mid-height
167 in proximity of the right end of the beam, Figure 7(a).

168 PB4P9 beam's crack map shows a longitudinal crack at the left beam's end in correspondence of strands'
169 depth due to splitting phenomena and spalling of concrete cover at the right end of the beam, Figure 9(a).

170 The crack map of the PB4P13 beam shows longitudinal cracks at both beam ends in correspondence of
171 strands' depth and swelling at the top of the beam which extended from the loading point to the right end of
172 the beam, Figure 10(a).

173 PB4P14 beam's crack map shows a longitudinal crack at the left beam end in close proximity to the cross-
174 section mid-depth, Figure 11(a).

175 3.3.2. Corrosion Level Detection

176 After the four-point bending tests, the prestressing strands were removed from the beams and cut in pieces,
177 500 mm long. The mass loss was measured by weighing the pieces after cleaning rust products. The clean-
178 ing was executed by using a 37% hydrochloric acid solution and a tank instrument with ultrasound energy.

179 The mass loss, η_s , was calculated according to Eq.(1):

$$\eta_s = \frac{m_0 - m}{m_0} \quad (1)$$

180 where m_0 is the mass per unit length of the uncorroded strand's piece and m is the final mass per unit length
181 of the strand's piece after cleaning.

182 Table 3 reports the three different levels of corrosion, which correspond to three value ranges of measured
183 mass loss. Level LVI - coloured in blue - corresponds to a low level of corrosion, level LVII - coloured in
184 green - corresponds to a medium level of corrosion, while level LVIII - coloured in red - corresponds to high
185 level of corrosion. The same colours in Figure 5(b) - Figure 11(b) indicate the strands' level of corrosion
186 along the length of PC beams.

187

188 4. RESULTS and DISCUSSION

189 In general, the shear resistance of PC beams without shear reinforcement and with corroded strands is af-
190 fected by the reduction of the transversal area of strands, the prestressing force and the bond between con-
191 crete and steel.

192 Two types of failure were experimentally observed at the end of the four-point bending tests, in the following
193 denoted as Shear I and Shear II.

194 Shear I failure mode was achieved after the formation of bending vertical cracks, perpendicular to the axis of
195 the beam, which developed at the bottom of the beam between the loading points where the constant value
196 of bending moment was applied. Afterward, shear diagonal cracks developed in the shear spans, in the re-
197 gions of constant shear force, from the bottom to the top of the beam. Finally, when cracks reached the load-
198 ing steel plate position, at the top of the beam, the beam collapsed, as shown in Figure 12(a).

199 Shear II failure mode was achieved after the formation of a single shear diagonal crack, that suddenly devel-
200 oped in correspondence of the more damaged shear spans of the beam; in this case bending vertical cracks
201 were not visible, as shown in Figure 12(b).

202 Shear I failure mode was more ductile than Shear II failure mode. Shear I failure mode could be anticipated
203 by the yielding of the strands, but flexural failures did not occur during the tests. According with the most re-
204 cent approaches adopted for the description of the mechanisms involved in the shear resistance of members
205 without transverse reinforcement (fib, 2013), the Shear I resistance of beams characterised by the same
206 shear span is decreasing as the corrosion level is increasing. Indeed, the corrosion of strands causes the
207 reduction of both transversal area of strands and prestressing force, which increases strains at mid-section
208 and descreases aggregate interlocking.

209 Both failure modes Shear I and Shear II occurred independently on shear span-to-depth ratios. Anyway, in-
210 teraction between shear and bending can be recognised as the shear span-to-depth ratio was varying,
211 (Leonhardt, 1965). In general, localised high levels of corrosion causes strain concentration and embrittle-
212 ment of the global response of the beam (Sanchez et al., 2017a; Sanchez et al., 2017b).

213 PBN4P2 uncorroded beam failed according to Shear I mode; from experimental outcomes of three points
214 bending tests, reported in Belletti et al. (2020), result that the flexural capacity of the uncorroded PC beams
215 was equal to 88 kNm. Since the interaction between shear force and bending moment is relevant in all the
216 analysed PC beams, Table 4 reports the values of the peak load, the maximum shear force, the bending mo-
217 ment, and the failure mode. PB4P5, PB4P6, PB4P8, PB4P13, and PB4P14 beams failed according to Shear
218 I mode after an initial development of vertical bending cracks, diagonal cracks occurred in correspondence of
219 shear spans, as shown in Figure 4, Figure 5(c), Figure 6(c), Figure 8(c), Figure 10(c), and Figure 11(c). Fig-
220 ure 4 shows that PBN4P2 beam's crack pattern at failure was almost symmetric with respect to the mid-span
221 of the beam. On the contrary, a more pronounced diagonal crack, which lead to the failure, developed in cor-
222 respondence of the shear span affected by the highest level of strands' corrosion in PB4P5, PB4P6, PB4P8,
223 PB4P13 and PB4P14 beams.

224 PB4P7 and PB4P9 beams failed according to Shear II mode after a sudden formation of a single shear diag-
225 onal crack, as reported in Figure 7(c) and Figure 9(c). PB4P7 beam failed on the side affected by the highest
226 level of corrosion; on the contrary PB4P9 beam failed on the opposite side. The crack patterns of PB4P7 and
227 PB4P9 beams show the formation of an extended horizontal crack at the strand's depth that may be caused
228 by bond failure. Indeed, it is well known that Kani's tooth model requires that bending moment, which is pro-
229 duced by bond force in strands, is in equilibrium with bending resistance of the cantilevered teeth, (Kani,
230 1966); Collins and Mitchell, 1991). Strand's debonding could be caused by splitting cracking induced by
231 dowel action mechanisms, which were activated for shear transfer. Indeed, in beams without transverse rein-
232 forcement, dowel action mechanism is limited by tensile strength of concrete, (Park et al., 1975). Figure 7(c)

233 and Figure 9(c) show that failure was suddenly achieved after the formation of splitting cracks at strand's
234 depth.

235 Shear I and Shear II failure modes depend not only on shear span-to-depth ratios, which were varying for the
236 tested beams, but also on the position and degree of strands' corrosion.

237 In general, for uncorroded RC beams there are two combined mechanisms to resist shear: beam action and
238 arch action. Beam action develops with variable tensile force at reinforcement (bond is needed) and almost
239 constant lever arm - if the beam has not stirrups, concrete tensile strength at the web is relevant. Arch action
240 develops with variable lever arm and constant tensile force at reinforcement (no bond) but an anchorage at
241 the end of the beam would be needed to bear the tie action in the arch. Experimental tests carried out by
242 Leonhardt (1965), on RC beams without web reinforcement and no damage, demonstrated that shear fail-
243 ures depend on shear span-to-depth ratios. For shear span-to-depth ratios ranging from 3 to 7, beam action
244 failure occurs at, or shortly after, the application of the diagonal cracking load; for shear span-to-depth ratios
245 ranging from 2 to 3, arch action failure occurs due to shear compression or flexural tension failure of the
246 compression zone above diagonal cracking load; for shear span-to-depth ratios lower than 2.5, arch action
247 failure occurs due to crushing/splitting of concrete. Thus, for shear span-to-depth ratios below 7, the flexural
248 capacity of the beams is not attained and shear governs the design (Park et al., 1975). The ranges of shear
249 span-to-depth ratios adopted for RC beams without web reinforcement cannot be directly used to schema-
250 tise the failure mode of the PC beams presented in this paper for several reasons. Firstly, the prestressing
251 force applied at a determinate eccentricity with respect to the center of the cross section generates additional
252 arch action mechanisms. Secondly, corrosion damage caused strain localisation that enables to easily sche-
253 matise the resisting mechanisms; indeed, resisting mechanisms can change or can reduce/increase their
254 effects along the beam length. Thirdly, loss of bond might have occurred, causing the reduction of beam ac-
255 tion and arch actions mechanisms. Finally, the decrease of compression concrete stresses, due to reduction
256 of prestressed force, has happened, weakening the shear performance.

257 **4.1. Load-Deflection curves**

258 Figure 13 shows experimental load-deflection curves of tested PC beams. Figure 13(a) shows that the ductil-
259 ity of PBN4P2 uncorroded PC beam is much higher than the ductility of corroded beams, not only because
260 this beam has the highest shear span-to-depth ratio (equal to 6.7) but also because stress localisation due to
261 corrosion effects did not occur. The ultimate mid-span deflection was equal to 120.70 mm, while the peak
262 load was equal to 98.47 kN.

263 A stiffer elastic response was expected for beams PB4P5 - PB4P9 because the shear span-to-depth was
264 ranging between 5.2 and 5.7. In reality, the strong reduction in corroded beams' ductility and resistance is
265 due not only to the lower shear span-to-depth ratios but also to corrosion effects. Figure 13(b)-(f) show that
266 the beneficial effect of prestressing on shear capacity of beams is strongly compromised by strands' corro-
267 sion. Furthermore, the reduced tensile resistance of strands caused a more pronounced interaction between
268 flexural and shear mechanisms. Indeed, where strands were corroded, higher flexural crack opening widths
269 developed causing detrimental effects on aggregate interlock mechanism, (Park et al., 1975).

270 Figure 13(g)-(h) show that load-deflection curves of PB4P13 and PB4P14 beams reached the highest shear
271 capacities and the lowest ultimate displacements because of the lowest shear span-to-depth ratios. Indeed,

272 according to Kani's comb model, cracked beams, having low values of shear span-to-depth ratios, can form
273 a tied arch that can support loads even after the failure of cantilevered teeth, (Collins and Mitchell, 1991).
274 PB4P5 and PB4P6 beams, both having shear span-to-depth ratios equal to 5.7, failed in Shear I mode in
275 correspondence of similar values of peak load - respectively equal to 90.21 kN and 89.39 KN - and ultimate
276 displacement at mid-span - respectively equal to 35.20 mm and 34.06 mm, Figure 13(b), (c). The higher level
277 of corrosion of PB4P6 beam caused a slightly lower resistance and ductility with respect to PB4P5 beam.
278 The shear span-to-depth ratios of PB4P7 and PB4P9 beams - equal to 5.5 and 5.4, respectively - were lower
279 than shear span-to-depth ratios of PB4P5 and PB4P6 beams. Therefore, lower ultimate displacement values
280 of PB4P7 and PB4P9 beams - respectively equal to 29.66 mm and 27.88 mm - than PB4P5 and PB4P6
281 beams were expected, Figure 13(d), (f). On the contrary, the lower peak load values of PB4P7 and PB4P9
282 beams - respectively equal to 81.74 kN and 80.00 kN - than PB4P5 and PB4P6 beams could be caused by
283 corrosion damage. Indeed, PB4P7 beam failed in correspondence of the shear span affected by the highest
284 level of strands' corrosion, while PB4P9 beam failed due to debonding on the side of the beam where spall-
285 ing of concrete cover was observed, Figure 13(d), (f).
286 PB4P8 beam, having a shear span-to-depth ratio equal to 5.2, failed in correspondence of a higher value of
287 the peak load - equal to 100.06 kN - than PB4P7 beam and a lower value of ultimate displacement - equal to
288 28.69 mm, Figure 13(e).
289 PB4P13 and PB4P14 beams, having the lowest values of shear span-to-depth ratios - respectively equal to
290 4.3 and 4.1 - failed in correspondence of the highest values of peak load - respectively equal to 127.45 kN
291 and 145.9 kN - and the lowest values of ultimate displacement - respectively equal to 23.7 mm and 22.3 mm,
292 Figure 13(g), (h).

293 **4.2. Principal strains field obtained from DIC**

294 Additional data on the principal strains field were obtained by performing DIC analyses after the experimental
295 test. The maximum principal strain values obtained using the DIC analyses were in good agreement with the
296 crack patterns observed during the tests. In Figure 13, the load-deflection curves are marked to identify the
297 load values corresponding to the contour plots of the maximum principal strain illustrated in Figure 14 - Fig-
298 ure 21. It is important to note that the contours' legends illustrated in Figure 14 - Figure 21 were not scaled
299 by using the same maximum value and the same number of intervals for all the beams. Anyway, for each
300 beam, the same legend is used to appreciate the crack pattern development. Figure 14 - Figure 21 con-
301 firmed that shear diagonal cracks developed always in correspondence of the shear span affected by the
302 highest level of corrosion detected along the strands, with the sole exception of PB4P9 beam who failed
303 probably due to strands' debonding, Figure 19.

304 Figure 14 - Figure 16, Figure 18 and Figure 20 - Figure 21 show the maximum principal strains measured
305 from photos of PBN4P2 - PBN4P6, PB4P8 beams and PB4P13 - PB4P14, revealing a Shear I failure mode .
306 These latter images reveal the presence of vertical bending cracks located in the central part of the beam,
307 where the bending moment its constant and reached the maximum value. As the load was increasing, the
308 vertical bending cracks increased their opening width values. Figure 14 and Figure 18 show the last contour
309 plots, recorded for an applied load equal to 95 kN and 100 kN, for PBN4P2 and PB4P8 beams respectively.
310 PBN4P2 and PB4P8 beams developed two shear diagonal cracks, which are approximately symmetric with
311 respect to the mid-span.

312 Figure 15 and Figure 16 show the principal strains evolution recorded from photos of PB4P6 and PB4P7,
313 respectively. The first images of the failure sequence highlight the presence of a vertical bending cracks in
314 correspondence of the bottom of the beam - when the applied load was equal to 75 kN. The last recorded
315 images, corresponding to a load equal to 90 kN and 85 kN respectively, reveal the formation of a wide shear
316 diagonal crack at the right and left side, respectively, where the highest levels of corrosion were found.
317 Figure 17 and Figure 19 show the principal strains evolution recorded from photos of PB4P7 and PB4P9
318 beams. During the tests, vertical bending cracks were not visible, while shear diagonal cracks were recorded
319 for the first time when the applied load was equal to 60 kN and 70 kN, for PB4P7 and PB4P9 beams, respec-
320 tively. The last recorded images of PB4P7 and PB4P9 beams, were taken in correspondence of an applied
321 load equal to 80 kN and 75 kN, respectively. Figure 17 and Figure 19 show the formation of a single shear
322 diagonal crack. In PB4P7 beam the diagonal crack develops in correspondence of the higher level of strands'
323 corrosion, while the failure of the beam PB4P9 occurred at the opposite side.
324 Figure 19 shows that for PB4P9 beam, whose failure was strongly affected by strands' debonding. The dis-
325 tance between supports and the first crack is lower than for other beams, meaning that prestressing force
326 value is lower in PB4P9 beam than in other beams. PB4P9 beam unexpectedly failed in the shear span - on
327 the right side of the beam - where corrosion was not detected but spalling of concrete cover was observed on
328 the right end of the beam which could cause detrimental effects on bond resistance.
329 Figure 20 and Figure 21 show the contour plots of maximum principal strains measured in PB4P13 and
330 PB4P14 beams, respectively. Figure 20 and Figure 21 show the formation of vertical cracks, which were not
331 visible to the naked eye during the experimental tests.

332 **4.3. Deformed shape of beams obtained from DIC**

333 Vertical displacements, obtained from DIC analyses, were useful to plot, the deformed shape of the beams
334 along their lengths in correspondence of different values of applied load, Figure 22. In general, the deformed
335 shape showed a parabolic trend, symmetric with respect to the mid-span of the beam where the maximum
336 value of vertical displacement was recorded. Similar profiles were obtained for all the tested specimens, ex-
337 cept for PB4P5, PB4P7, and PB4P9 beams. Indeed, PB4P5, PB4P7, and PB4P9 beams were characterised
338 by an un-symmetric profile of the deformed shape and a strong displacement localisation where shear diago-
339 nal cracks occurred. This discontinuity of the beams' deformed shape could be due to bond failure. Indeed
340 horizontal cracks, which formed at strand's depth, were visible to the naked eye in PB4P5, PB4P7 and
341 PB4P9 beams, Figure 5, Figure 7, and Figure 9. Figure 22(b), Figure 22(d), and Figure 22(f) show that,
342 where splitting horizontal cracks developed - in PB4P5, PB4P7, and PB4P9 beams - a strong increase of
343 vertical displacements was observed. The localised increment of vertical displacement values could be due
344 to a localised strong stiffness reduction caused by strands' debonding. Strand's debonding could be caused
345 by a mix of reasons affecting the shear transfer, such as splitting of concrete induced by rust volume expan-
346 sion, reduction of tensile force in strands induced by mass loss or dowel action effects on concrete cover.

347 **5. CONCLUSIONS**

348 In this paper, the results of experimental tests on seven naturally corroded PC beams and one uncorroded
349 control PC beam are presented and discussed. In order to investigate the shear capacity dependency on

350 corrosion effects, four-point bending tests were carried out up to failure. Finally, the main outcomes from vis-
351 ual inspection, as crack pattern maps and mass loss weighing, have been correlated to observed shear fail-
352 ures and measurements of displacements.

353 According to the results obtained from the experimental tests, the following conclusions are listed:

- 354 • In general, the beams were characterised by different shear span-to-depth ratios, therefore results
355 observed for the uncorroded PC beam cannot be directly compared with the results obtained for the
356 corroded PC beams.
- 357 • The strands' corrosion caused strain localisations and premature failure modes. Shear resistance of
358 beams characterised by similar shear span-to-depth ratios decreased as the corrosion level of the
359 strands increased.
- 360 • The beneficial effect of prestressing on shear capacity of beams was strongly compromised by strands'
361 corrosion. Indeed, the reduced tensile resistance of corroded strands caused a more pronounced
362 interaction between flexural and shear mechanisms.
- 363 • The zones of the PC beams affected by higher level of corrosion were potential zones where higher
364 diagonal crack opening widths developed causing detrimental effects on aggregate interlock
365 mechanism.
- 366 • Lastly, this experimental campaign demonstrates that the knowledge of the corrosion level distribution
367 over the length of PC members is fundamental for a reliable prediction of the effects of strain
368 localisation on the non-linear behaviour of structures and infrastructures. Indeed, well established
369 mechanisms, such as beam action or arch action, which are used for schematise the shear transfer of
370 RC beams, need to be modified in order to consider the localisation effects produced by corrosion in PC
371 beams.

372

373 **ACKNOWLEDGEMENTS**

374 The authors are grateful to the members of the Structural Laboratory of the Institute of Construction Sci-
375 ences "Eduardo Torroja" of CSIC of Spain for help in all the instrumentation and the facilities to test the
376 beams (PIE 201860E005). Furthermore, they are grateful to Alessandro Corrente of the Faculty of Engineer-
377 ing of University of Parma who followed the experimental test during his Master Thesis. Finally, this paper
378 reports a part of the scientific results obtained by the University of Parma within the PRIN project (Italian Re-
379 search Project of Prominent National Interest): "Failure mechanisms due to lack of construction details and
380 degradation phenomena in existing reinforced concrete structures" financially co-founded by MIUR (Italian
381 Ministry of Education, University and Research).

382

383 **References**

384 Belletti B., Andrade C., Franceschini L., Montero J.S., Vecchi F., 2020. Prestressed beams exposed to natural
385 chloride action studied through flexural tests and Digital Image analysis. *Submitted for publication.*

386 Belletti B., Vecchi F., Bandini C., Andrade C., Montero J.S. 2019. Numerical evaluation of the corrosion effects
387 in prestressed concrete beams without shear reinforcement. *Structural Concrete*, online
388 <https://doi.org/10.1002/suco.201900283>.

389 Blaber J., Adair B., Antoniou A., 2015. Ncorr: open-source 2D digital image correlation MATLAB software.
390 *Experimental Mechanics*, **55**(6): 1105-1122.

391 Cavagnis F., Ruiz M. F., Muttoni A. (2018). A mechanical model for failures in shear of members without
392 transverse reinforcement based on development of a critical shear crack. *Engineering structures*, **157**:
393 300-315.

394 Classen M., 2020. Shear Crack Propagation Theory (SCPT)–The mechanical solution to the riddle of shear in
395 RC members without shear reinforcement. *Engineering Structures*, **210**, 110207.

396 Collins, M.P. and Mitchell, D., 1991. Prestressed Concrete Structures. Prentice Hall, Englewood Cliffs.

397 CONTECVET IN30902I, 2001. A validated user's manual for assessing the residual life of concrete structures,
398 DG Enterprise, CEC, available on-line: www.ietcc.csic.es or www.geocisa.es.

399 Di Prisco M., 2019. Critical Infrastructures in Italy: State of the Art, Case Studies, Rational Approaches to
400 Select the Intervention Priorities. *Proceedings of the fib Symposium: Concrete - Innovations in Materials,*
401 *Design and Structures*, Krakow, Poland; 27-29 May: 49-58.

402 fib – International federation for structural concrete. fib model code for concrete structures 2010. 431 Ernst &
403 Sohn; 2013; 434 p.

404 Higgins C., Farrow W. C., 2006. Tests of Reinforced Concrete Beams with Corrosion-Damaged Stirrups. *ACI*
405 *Structural Journal*, **103**(1): 133-141.

406 Juarez C.A., Guevara B., Fajardo G., Castro-Borges P., 2011. Ultimate and Nominal Shear Strength in Rein-
407 forced Concrete Beams Deteriorated by Corrosion. *Engineering Structures*, **33**(12): 3189-3196.

408 Kani G.N.J., 1966. Basic Facts Concerning Shear Failure. *Journal ACI*, **63**: 675-692.

409 Lachemi M., Al-Bayati N., Sahmaran M., Anil O., 2014. The Effect of Corrosion on Shear Behavior of Rein-
410 forced Self-Consolidating Concrete Beams. *Engineering Structures*, **79**: 1-12.

411 Leonhardt F., 1965. Reducing the Shear Reinforcement in Reinforced Concrete Beams and Slabs. *Magazine*
412 *of Concrete Research*, **17**(53): 187-198.

413 Marí, A., Bairán, J., Cladera, A., Oller, E., & Ribas, C. 2015. Shear-flexural strength mechanical model for the
414 design and assessment of reinforced concrete beams. *Structure and Infrastructure Engineering*, **11**(11),
415 1399-1419.

416 Mora L.S., Andrade C., Belletti B., Vecchi F., Zambonini S., Santiago J.R., Montero J.S. 2019. Corrosion effects
417 in prestressed concrete beams: Experimental test and non-linear finite element analysis. fib Symposium
418 2019: Concrete - Innovations in Materials, Design and Structures. Krakow, Poland; 27 - 29 May: 905-
419 912

420 Mora L.S., Zambonini S., De La Peña D., Gonzalez Ocampos I., Andrade C., Belletti B., Rodriguez J.S., Mon-
421 tero J., 2018. Interacción Numérico-Experimental entre el Comportamiento Complejo de Materiales y
422 Modelos a Gran Escala de Elementos de Hormigón Armado. International Conference on Construction
423 Research AEC, Madrid, Spain.

424 Park R., Paulay T., 1975. Reinforced Concrete Structures. John Wiley and Sons, New York, N.Y

425 Recupero A., Spinella N., 2019. "Experimental test on corroded prestressed concrete beams subjected to
426 transverse load". *Structural Concrete*, **20**: 2220-2229.

427 Rinaldi Z., Imperatore S., Valente C., 2010. Experimental evaluation of the flexural behavior of corroded P/C
428 beams. *Construction and Building Materials*, **24**: 2267-2278.

429 Rodriguez J., Ortega L.M., Casal J., 1997. Load carrying capacity of concrete structures with corroded rein-
430 forcement. *Construction and Building Materials*, **11**(4): 239-248.

431 Sanchez J., Fullea, J., Andrade C., 2017a. Corrosion-induced brittle failure in reinforcing steel, *Theor. Appl.*
432 *Fract. Mech.* **92**: 229–232.

433 Sanchez J., Fullea, J., Andrade C., 2017b. Fracto-surface mobility mechanism in high-strength steel wires,
434 *Eng. Fract. Mech.* **186**: 410–422.

435 Schreier, H., Orteu, J.-J., Sutton, M.A., 2009. Image Correlation for Shape, Motion and Deformation Measure-
436 ments: Basic Concepts, Theory and Applications. Springer.

437 Soltani M., Safiey A., Brennan A., 2019. A State-of-the-Art Review of Bending and Shear Behaviors of Corro-
438 sion-Damaged Reinforced Concrete Beams. *ACI Structural Journal*, **116**(3): 53-64.

439 Tambusay A., Suryanto B., Suprobo P., 2018. Visualization of shear cracks in a reinforced concrete beam
440 using the Digital Image Correlation. *International Journal on Advanced Science Engineering Information*
441 *Technology*, **8**(2): 573-578.

442 Woodward, R. J., & Williams, F. W., 1988. Collapse of Ynys-y-Gwas bridge, West Glamorgan. *Proceedings of*
443 *the Institution of Civil Engineers Part 1*, **84**: 635–669.

444 Zhou Y., Gentcturk B., William K., Attar A., 2014. Carbonation-Induced and Chloride-Induced Corrosion in
445 Reinforced Concrete Structures. *Journal of Materials in Civil Engineering*, **27**(9): 1-16

446

447 **List of Tables**

448

449 **Table 1** Steel mechanical properties.

Type of reinforcements	Diameter [mm]	Yield strength [MPa]	Modulus of elasticity [GPa]	Ultimate strain [%]
Rebars	5	435	195	18
Strands	12.9	1580	195	5

450

451







452 **Table 2** Details of the loading setup.

Specimens	Configuration	L [mm]	d ₁ [mm]	d ₂ [mm]	a/d
PBN4P2	4 Point Bending	5040	200	200	6,7
PB4P5	4 Point Bending	4260	980	200	5,7
PB4P6	4 Point Bending	4240	200	1000	5,7
PB4P7	4 Point Bending	4100	200	1140	5,5
PB4P8	4 Point Bending	3900	1340	200	5,2
PB4P9	4 Point Bending	4060	950	200	5,4
PB4P13	4 Point Bending	3210	1000	1000	4,3
PB4P14	4 Point Bending	3110	1100	1000	4,1

453

454

455 **Table 3** Corrosion levels, mass loss, and strand samples.

Corrosion Level	Corrosion pattern colour	Mass loss	Samples
LVI		$\eta_s < 2 \%$	
LVII		$2 < \eta_s < 10 \%$	
LVIII		$\eta_s > 10 \%$	

456

457 **Table 4** Main experimental results: peak load, shear, moment, and failure mode.

Beam	a/d	Peak load [kN]	Shear force [kN]	Bending moment [kNm]	Failure mode
PBN4P2	6,7	98.47	49.24	82.71	Shear I
PB4P5	5,7	90.21	45.11	64.05	Shear I
PB4P6	5,7	89.39	44.70	63.17	Shear I
PB4P7	5,5	81.74	40.87	55.86	Shear II
PB4P8	5,2	100.06	50.03	65.04	Shear I

PB4P9	5,4	80.00	40.00	54.13	Shear II
PB4P13	4,3	127.45	63.73	68.19	Shear I
PB4P14	4,1	145.90	72.95	75.62	Shear I

458
459

460

461 **Figure captions**

462 Figure 1. Cross-section of the beams and longitudinal reinforcements.

463 Figure 2. Damage induced by corrosion of strands: (a) strands' corrosion, (b) spalling of concrete cover, (c)
464 swelling, and (d) longitudinal crack.

465 Figure 3. Test setup configuration: (a) four-point bending and region of interest (ROI), and (b) hydraulic actu-
466 ator.

467 Figure 4. PBN4P2 beam at failure.

468 Figure 5. Beam PB4P5: (a) crack pattern map before the test, (b) corrosion level pattern, and (c) photo at
469 failure.

470 Figure 6. Beam PB4P6: (a) crack pattern map before the test, (b) corrosion level pattern, and (c) photo at
471 failure.

472 Figure 7. Beam PB4P7: (a) crack pattern map before the test, (b) corrosion level pattern, and (c) photo at
473 failure.

474 Figure 8. Beam PB4P8: (a) crack pattern map before the test, (b) corrosion level pattern, and (c) photo at
475 failure.

476 Figure 9. Beam PB4P9: (a) crack pattern map before the test, (b) corrosion level pattern, and (c) photo at
477 failure.

478 Figure 10. Beam PB4P13: (a) crack pattern map before the test, (b) corrosion level pattern, and (c) photo at
479 failure.

480 Figure 11. Beam PB4P14: (a) crack pattern map before the test, (b) corrosion level pattern, and (c) photo at
481 failure.

482 Figure 12. Shear failure modes: (a) Shear I failure mode - PB4P5 beam - and (b) Shear II failure mode -
483 PB4P7 beam.

484 Figure 13. Load-deflection curves: (a) PBN4P2, (b) PB4P5 and (c) PB4P6, (d) PB4P7, (e) PB4P8, (f) PB4P9,
485 (g) PB4P13, and (h) PB4P14.

486 Figure 14. DIC of beam PBN4P2.

487 Figure 15. DIC of beam PB4P5.

488 Figure 16. DIC of beam PB4P6.

489 Figure 17. DIC of beam PB4P7.

490 Figure 18. DIC of beam PB4P8.

491 Figure 19. DIC of beam PB4P9.

492 Figure 20. DIC of beam PB4P13.

493 Figure 21. DIC of beam PB4P14.

494 Figure 22. Vertical displacement along the beam length for different load values: (a) PBN4P2, (b) PB4P5, (c)
495 PB4P6, (d) PB4P7, (e) PB4P8, (f) PB4P9, (g) PB4P13, and (h) PB4P14.
496